Color-Tunable Upconversion Emission Switch Based on Cocrystal-to-Cocrystal Transformation

Yu Wang,[1] Huang Wu,[1,*] Leighton O. Jones,[1] Martín A. Mosquera,[2] Charlotte L. Stern,[1] George C. Schatz[1] and J. Fraser Stoddart[1,3,4,5,6,*]

[1]*Department of Chemistry, Northwestern University, 2145 Sheridan Road, Evanston, Illinois 60208, United States*

[2]*Department of Chemistry and Biochemistry, Montana State University, 103 Chemistry and Biochemistry Building, Bozeman, Montana 59717, United States*

[3]*School of Chemistry, University of New South Wales, Sydney, NSW 2052, Australia*

[4]*Stoddart Institute of Molecular Science, Department of Chemistry, Zhejiang University, Hangzhou 310027, P. R. China*

[5]*ZJU-Hangzhou Global Scientific and Technological Innovation Center, Hangzhou 311215, China*

[6]*Lead Contact*

**Correspondence: huang.wu@northwestern.edu; stoddart@northwestern.edu*

SUMMARY

Cocrystal engineering, involving the co-assembly of two or more components into a highly ordered solid-state superstructure, has emerged as a popular strategy to tune the photophysical properties of crystalline materials. The reversible co-assembly and disassembly of multicomponent cocrystals, as well as their reciprocal transformation in the solid state remain a challenging objective. Herein, we have reported a color-tunable upconversion emission switch based on the invertible transformation between two cocrystals. One red- and one yellow-emissive cocrystals, composed of an electron-deficient naphthalenediimide-based triangular macrocycle and different electron donors, have been synthesized. The red-emissive cocrystal and yellow-emissive cocrystal undergo reversible transformation by exchanging their electron donors. Benefiting from intermolecular charge transfer interactions, the two cocrystals display improved two-photon excited upconversion emission. Accompanying the reversible transformation of two cocrystals, their upconversion emission color changes between red and yellow, forming a dual-color upconversion emission switch. This work provides a rare example of precise control of cocrystal-to-cocrystal transformation, and affords a reference for fabricating color-tunable nonlinear optical materials in the solid state.

KEY WORDS: Cocrystal Engineering, Charge Transfer, Organic Macrocycles, Supramolecular Assembly, Tunable Emission, Multiphoton Absorption

INTRODUCTION

Organic cocrystals,[1-3] on account of their simple preparation, well-defined superstructures and diverse functions, have kindled considerable interest in supramolecular chemistry[4-7], biomedical engineering[8,9] and materials science[10-12]. Cocrystals can be prepared by vapor-phase,[11] liquid-phase,[13,14] and solid-phase methods,[15] methods which are low cost, convenient and feasible, as well as avoiding tedious covalent synthesis. With ordered superstructures, organic cocrystals serve[16-18] as promising candidates for investigating superstructure-property relationships. Generally, cocrystals exhibit[19] multifunctional properties as they integrate the properties of different precursors. They display[20,21] innovative properties that differ from their precursors on some occasions, such as metallic electrical conductivity,[22] ambipolar charge transport,[23] room-temperature ferroelectricity,[24] nonlinear optical response,[25] and room-temperature phosphorescence[26]. Moreover, with dynamic and reversible intermolecular noncovalent binding interactions, cocrystals exhibit[27-30] dynamic reversibility and stimuli responsiveness, which makes them promising candidates for intelligent materials. The co-assembly behavior during the fabrication of cocrystals, however, remains uncontrolled and unpredictable, making it difficult to customize specific cocrystals, not to mention realizing a reversible transformation between multicomponent cocrystals.

Endowing organic cocrystals with excellent optical properties is[31-33] a worthwhile goal for materials scientists. Crystalline luminescent materials with tunable fluorescent colors have been developed,[34] because of their potential applications in visual displays, multiplexed bioimaging, data encryption and data storage devices.[35-38] Their emission colors can be tuned by changing the precursor molecules,[39] controlling the stoichiometric ratio of different precursors,[40] altering the molecular packing modes,[41] and doping another component.[42] In contrast to luminescent materials with one-photon absorption, upconversion emission materials, which enable conversion[43] of low-energy photons into high-energy photons, have attracted[44-46] widespread attention. They possess[47] unique advantages including large penetration depth, low optical scattering, and high spatial resolution. Constructing crystalline luminescent materials, which integrate the features of wavelength tunability and upconversion emission, is an attractive research objective.

Herein, we have demonstrated (Scheme 1) a reversible color-tunable upconversion emission switch based on the transformation of two charge transfer cocrystals. They are composed of the same electron acceptor—a naphthalenediimide-based triangular macrocycle **NDI-Δ**[48]. With 9, 10-dichloroanthracene (**DCA**) and 1-chloronaphthalene (**CN**) as the electron donor, the two

cocrystals **DCA·NDI-Δ** and **CN·NDI-Δ** have been obtained, and these exhibit red and yellow fluorescence, respectively. Single-crystal X-ray diffraction analyses reveal that the **DCA·NDI-Δ** cocrystal adopts a porous solid-state superstructure with a large guest-accessible volume, while **CN·NDI-Δ** has a condensed superstructure. The porous red-emissive **DCA·NDI-Δ** cocrystal can transform into the yellow-emissive **CN·NDI-Δ** cocrystal by drop casting of **CN** molecules, and then recovery by the removal of the volatile **CN** molecules through solvent vapor annealing. This reversible cocrytal-to-cocrystal transformation has been investigated by fluorescence microscopy, powder X-ray diffraction analyses, and Raman spectroscopy. Multi-photon microscopic experiments reveal that the two cocrystals exhibit strong two-photon excited fluorescence. Their red and yellow upconversion emission can be switched when accompanied by the cocrystal transformation, leading to the formation of a color-tunable upconversion emission switch.

RESULTS AND DISCUSSION

Growth of DCA·NDI-Δ and CN·NDI-Δ Cocrystals

The triangular macrocycle **NDI-Δ**, containing three electron-deficient naphthalenediimide (NDI) units, serves[49] as a good electron acceptor. It enables binding to electron-rich molecules through outer surface interactions, forming charge transfer complexes. With a shape-persistent triangular geometry, **NDI-Δ** is a vital building block to construct[50] a variety of supramolecular architectures, *e.g.*, single-handed helices, one-dimensional (1D) supramolecular nanotubes, and two-dimensional (2D) supramolecular tessellation patterns. Its diverse assembly behaviors in the solid state indicate that it holds great promise for constructing charge transfer cocrystals with exquisite superstructures. The π-conjugated NDI units[40,51,52] also imbue **NDI-Δ** with a wealth of photophysical properties, making it a good candidate for building solid-state optical materials.

With **NDI-Δ** as the electron acceptor, two cocrystals with distinct emission colors based on different electron donor molecules have been synthesized. 9, 10-Dichloroanthracene (**DCA**), with good optical properties,[53,54] is selected as one electron donor. The **DCA·NDI-Δ** cocrystal is obtained by slow vapor diffusion of MeOH into a CH_2Cl_2 solution of **NDI-Δ** and **DCA**. The optical (Figures 1A and S15) and scanning electron microscopic (SEM, Figure S16) images reveal that the **DCA·NDI-Δ** cocrystals have a 2D quadrangular shape with lengths ranging from a few to tens of micrometers. 1-Chloronaphthalene (**CN**), with a small molecular size and easily volatile nature,[55] is employed as another electron donor. The **CN·NDI-Δ** cocrystal is obtained

by slow vapor diffusion of MeOH into the PhCl solution of **NDI-Δ** and **CN**. It exhibits (Figures 1B and S17) 1D rod-like morphology with lengths up to a few tens of micrometers.

The formation of two cocrystals, **DCA·NDI-Δ** and **CN·NDI-Δ**, can be observed (Figure S14) by naked eye on account of the dramatic color change. **NDI-Δ** and **DCA** crystals are white and yellow, while the **DCA·NDI-Δ** cocrystal is red and the **CN·NDI-Δ** cocrystal is yellow. The formation of the **DCA·NDI-Δ** cocrystal has been confirmed by powder X-ray diffraction (PXRD) analysis, Raman spectroscopy, and SEM-equipped energy-dispersive X-ray spectroscopy (SEM-EDS). The PXRD pattern of the **DCA·NDI-Δ** cocrystal shows (Figure S13) a new set of diffraction peaks, which are different from those for its precursors, indicating the formation of a new solid-state superstructure. The Raman spectrum of **DCA·NDI-Δ** cocrystal includes (Figure S18) the characteristic peaks for **DCA** (1269, 1478, 1547 cm^{-1}), and the vibrational peaks for **NDI-Δ** (1420, 1606, 1719 cm^{-1}). SEM-EDS Analysis for the **DCA·NDI-Δ** cocrystal shows (Figure S16) that the component elements of donor and acceptor molecules, including carbon, nitrogen, oxygen, and chlorine, are distributed homogeneously throughout the entire microcrystal. All these results demonstrate the formation of a multicomponent cocrystal **DCA·NDI-Δ** based on charge transfer interactions between the electron-deficient **DCA** and the electron-rich **NDI-Δ**. The synthesis of the **CN·NDI-Δ** cocrystal has also been confirmed by PXRD patterns (Figure S13), Raman spectra (Figure S18) and SEM-EDS analysis (Figure S17). These results suggest that two macrocycle-based cocrystals have been obtained successfully by the co-assembly of **NDI-Δ** with two different electron donor molecules.

Photophysical Properties

With different electron-donating precursors, the **DCA·NDI-Δ** and **CN·NDI-Δ** cocrystals display distinctive optical properties. The fluorescence microscopic images indicate (Figure 1A and 1B) that the **DCA·NDI-Δ** and **CN·NDI-Δ** cocrystals exhibit red and yellow luminescence, respectively. In order to elucidate their photophysical properties, solid-state UV-Vis absorption and fluorescence spectra were recorded. The spectra reveal that the absorption bands of the **NDI-Δ** and **DCA** crystals are (Figure 1C) in the region of 250−420 and 250−460 nm, respectively. The **DCA·NDI-Δ** cocrystal shows (Figure 1C) a broad absorption band with a wavelength extended up to 593 nm, which is bathochromically shifted by over 130 nm in comparison with those of **NDI-Δ** and **DCA**. The solid-state absorption spectrum of the **CN·NDI-Δ** cocrystal (Figure 1C) reveals a wide absorption band ranging from 250 to 505 nm, which is ~85 nm red-shifted compared to that of **NDI-Δ**. These red-shifted absorption bands of

the **DCA·NDI-Δ** and **CN·NDI-Δ** cocrystals arise from intermolecular charge transfer interactions between electron donor and acceptor molecules. Optical gaps of the cocrystals can be calculated based on their absorption edges. The results disclose that the gap for **DCA·NDI-Δ** is 2.09 eV, which is narrower than that (2.46 eV) for **CN·NDI-Δ**. This may arise from the stronger electron donating ability of **DCA** than that of **CN**.

The **DCA·NDI-Δ** and **CN·NDI-Δ** cocrystals display red-shifted emission compared to their precursors, an observation which is similar to their absorption spectra. The emission band of **NDI-Δ** crystal is (Figure 1D) centered on 490 nm, while two emission peaks at 465 and 485 nm are observed (Figure 1D) in the fluorescence spectrum of **DCA** crystal. **DCA·NDI-Δ** cocrystal exhibits (Figure 1D) a deep-red emission at 645 nm, which is significantly red-shifted by 155 nm in comparison with that of the **NDI-Δ** crystal. **CN·NDI-Δ** cocrystal shows yellow fluorescence with an emission peak at 547 nm, demonstrating a red shift of 57 nm compared with that of **NDI-Δ** crystal. These significant bathochromic shifts observed in the fluorescence spectra indicate that cocrystallization can serve as an effective tool to tune solid-state luminescence. Compared with **CN·NDI-Δ**, **DCA·NDI-Δ** displays more red-shited absorption and emission, demonstrating that the electron-donating molecules play a critical role in tuning the photophysical properties of cocrystals.

Solid-State Superstructures

Single-crystal X-ray diffraction analyses were performed in order to investigate the intermolecular noncovalent interactions in the two donor-acceptor cocrystals and reveal their superstructure-photophysical property relationships. The **DCA·NDI-Δ** cocrystal adopts(Table S1) a trigonal *R*32 space group with a donor-acceptor stoichiometry of 1:1. Three **DCA** molecules stack (Figure 2A and 2C) face-to-face with three NDI units in **NDI-Δ** by means of [π···π] interaction with a distance of 3.26 Å. Additionally, the chlorine atoms in **DCA** have close contacts with the cyclohexano hydrogen atoms and the NDI unit in **NDI-Δ** with [Cl···H–C] and [Cl···π] distances of 2.79 and 3.30–3.36 Å, respectively. Surrounded by **DCA** molecules, two adjacent **NDI-Δ** macrocycles stack (Figure 2B and 2D) in a coaxial manner with a rotation angle of 60°, stabilized by multiple [C−H···O] hydrogen bonds with a distance of 2.39 Å. Independent gradient model (IGM) analysis[56,57] provides (Figure S7−9) a visual understanding of these noncovalent binding interactions. Every **DCA** molecule interacts (Figures 2E and S10) with two **NDI-Δ** macrocycles held together by multiple [π···π], [Cl···π] and [Cl···H–C] interactions. Stabilized by these synergetic noncovalent interactions, six **DCA** molecules and six **NDI-Δ** molecules stack (Figures 2E and S10) around a vertex, forming a uniform hexagonal

superstructure in the *a*−*b* plane. There is a pore in the center of the supramolecular hexagon with a diameter of 11.16 Å. Consequently, the **DCA·NDI-Δ** cocrystal adopts a porous superstructure, wherein the guest-accessible voids account for 36.3% of the whole crystal.

The solid-state superstructure of **CN·NDI-Δ** reveals that the cocrystal crystallizes (Table S1) in a monoclinic $P2_1$ space group. The three NDI units in **NDI-Δ** interact (Figure 3A and 3C) with three **CN** molecules through face-to-face [π···π] interactions with distances ranging from 3.21 to 3.37 Å. Each **NDI-Δ** macrocycle is surrounded by another three **CN** molecules sustained by the [C−H···π] interactions between the cyclohexano hydrogen atom in **NDI-Δ** and the plane of **CN**. The **NDI-Δ** macrocycles stack into a 1D columnar superstructure (Figure S5) along the *a* axis, wherein adjacent **NDI-Δ** macrocycles connect (Figure 3B and 3D) with each other in a coaxial manner by means of multiple [C−H···O] hydrogen bonds with distances of 2.42–2.46 Å. These noncovalent interactions are visualized (Figures S11 and S12) by IGM analysis. **NDI-Δ** macrocycles in neighboring 1D columns are held (Figure S5) together by six **CN** molecules, forming a vertex-to-edge tiling pattern in the *b*–*c* plane. The lattice space between the interlayer of the vertex-to-edge tiling pattern is almost filled up (Figure 3E) by small **CN** molecules, therefore, **CN·NDI-Δ** possesses a condensed superstructure.

These single-crystal analyses reveal that the electron-deficient **NDI-Δ** macrocycle prefers to interact with electron donor molecules through outer surface [π···π] interactions. **DCA·NDI-Δ** cocrystal adopts a porous superstructure with a large guest-accessible void fraction. In contrast, **CN·NDI-Δ** cocrystal has a condensed cocrystal superstructure, on account of the small molecular size of **CN** molecules. These results indicate that the superstructures of cocrystals are highly dependent on the sizes and shapes of their electron donors.

Frontier Molecular Orbitals Calculations

The density functional theory (DFT) calculations based on the solid-state superstructures of **DCA·NDI-Δ** and **CN·NDI-Δ** cocrystals were carried out in order to investigate the difference in photophysical properties of the two cocrystals. The LUMOs of the **DCA·NDI-Δ** and **CN·NDI-Δ** cocrystals are (Figures 4, S28 and S29) concentrated on the electron acceptor **NDI-Δ**, and hence **DCA·NDI-Δ** and **CN·NDI-Δ** have similar LUMO energies of −3.57 and −3.68 eV, respectively. The HOMOs of the two cocrystals are localized on the electron-donating molecules. Since **DCA** possesses (Figure 4) a higher HOMO energy of −5.36 eV compared to that (−5.80 eV) for **CN**, the cocrystal **DCA·NDI-Δ** has a higher HOMO energy of −5.49 eV compared to that (−5.99 eV) for **CN·NDI-Δ**. The HOMO-LUMO energy gaps (Δ*E*)

of **DCA·NDI-Δ** and **CN·NDI-Δ** are (Figures 4, S28 and S29) calculated to be 1.92 and 2.31 eV, respectively, values which are in agreement with those obtained ($\Delta E = 2.09$ and 2.46 eV for **DCA·NDI-Δ** and **CN·NDI-Δ**, respectively) from their UV-Vis absorption spectra. The narrower energy gap of **DCA·NDI-Δ** in comparison with **CN·NDI-Δ** indicates the origin of the more red-shifted absorption and emission spectra of **DCA·NDI-Δ**. These results demonstrate that the bandgaps of cocrystals are mainly determined by the HOMO of electron donors and the LUMO of electron acceptors, and their photophysical properties can be modulated effectively by tuning the energy levels of donors and acceptors. It provides a reference to the tailor optical properties of cocrystals, laying a foundation to construct wavelength-tunable luminescent crystalline materials.

Reversible Cocrystal-to-Cocrystal Transformation

The porous superstructure of **DCA·NDI-Δ** with a large guest-accessible void fraction provides a good platform to explore the cocrystal-to-cocrystal transformation (Figure 5A). A **DCA·NDI-Δ** film has been fabricated by dropping a suspension of the **DCA·NDI-Δ** cocrystal in MeOH on a glass substrate followed by air drying. When a **CN** solution in MeOH (CN/MeOH = 1:9 v/v) is dropped on the surface of the **DCA·NDI-Δ** film (Figure S31), the fluorescent color of the film undergoes a significant change, with the evaporation of the droplet. Its original red emission at 645 nm (Figure 5B and 5E) changes (Figure 5C and 5F) gradually into yellow emission with a peak centered on 548 nm. The corresponding fluorescence spectrum of the film is in accordance with that of the **CN·NDI-Δ** cocrystal, indicating the formation of a **CN·NDI-Δ** cocrystal in the film. The yellow emission of the transformed film can go back to red emission if triggered by solvent vapor annealing (Figure S31).[58] Upon exposure of the yellow-emissive film to the vapor of boiling CH_2Cl_2, the fluorescence of the film recovers (Figure 5D and 5G) to the initial red emission with a peak at 644 nm, an observation which implies restitution of the **DCA·NDI-Δ** cocrystal. Overall, the emission color of the film can undergo reversible changes between red and yellow upon introducing **CN** molecules by drop casting and its removal by solvent vapor annealing, leading to the formation of a high-contrast dual-color fluorescent switch. This reversible fluorescent switch may be attributed to a cocrystal-to-cocrystal transformation (Figure 5A) between **DCA·NDI-Δ** and **CN·NDI-Δ**.

PXRD Analysis has been carried out to verify the reversible cocrystal transformation. After the **DCA·NDI-Δ** film transformed into the yellow-emissive one, the original PXRD peaks for the **DCA·NDI-Δ** cocrystal disappear (Figure 5H), and meanwhile a new set of diffraction peaks occurs. The resulting PXRD pattern is consistent (Figure 5H) with that of the **CN·NDI-Δ**

cocrystal, demonstrating the transformation from **DCA·NDI-Δ** film to **CN·NDI-Δ** film. This observation indicates that **CN** molecules are able to replace **DCA** molecules to cocrystalize with **NDI-Δ** in the solid state. When the yellow-emissive film recovers to the red-emissive one upon solvent vapor annealing, the characteristic PXRD peak for the **DCA·NDI-Δ** cocrystal is observed (Figure 5H), suggesting the **CN·NDI-Δ** film changes back to the **DCA·NDI-Δ** film. These results indicate that these two cocrystals undergo reversible transformation upon alternating drop casting and solvent vapor annealing. This cocrystal transformation has also been confirmed by Raman spectroscopy. The vibrational peaks for **DCA·NDI-Δ** film at 1269, 1478, 1547 cm^{-1} disappear (Figure 5I) upon drop casting of the **CN** solution, and reappear after solvent vapor annealing. These results suggest that a cocrystal-to-cocrystal transformation based on the exchange of electron donor molecules has been achieved successfully, providing a rare example of dynamic modulation of the solid-state superstructures of cocrystals.

Based on theoretical calculations and superstructures of the two cocrystals, we propose a possible process for the cocrystal transformation. **DCA·NDI-Δ** adopts a porous superstructure with a relative high guest-accessible void fraction of 36.3%. When the **CN** solution in MeOH is dropped on the surface of **DCA·NDI-Δ** film, the small **CN** molecules (Figure S6) are able to diffuse into the voids of **DCA·NDI-Δ** film by physical absorption. Assuming that the total binding energy between **NDI-Δ** and **CN** molecules is higher than that between **NDI-Δ** and **DCA** molecules, **CN** molecules will gradually replace the **DCA** molecules within the film. Consequently, the **DCA·NDI-Δ** film gradually transforms into the more stable **CN·NDI-Δ** film, leading to the release of **DCA** molecules that are distributed disorderedly throughout the film. Upon exposure of the transformed **CN·NDI-Δ** film to the vapor of boiling CH_2Cl_2, **CN** molecules will be removed by the rising CH_2Cl_2 vapor from the film on account of the volatile nature of **CN** molecules. The **DCA** and **NDI-Δ** molecules in the film will rearrange in the atmosphere of the CH_2Cl_2 vapor, leading to the regeneration of **DCA·NDI-Δ** cocrystal.

Commented [GS1]: This makes it sound like the vapor assists transport. Do you understand the mechanism? It seems like this is a key point in the mechanism, and yet it isn't clear what involved.

Color-Tunable Upconversion Emission

Due to intermolecular charge transfer interactions between electron donor and acceptors,[59] the **DCA·NDI-Δ** and **CN·NDI-Δ** cocrystals emerge as having good nonlinear optical response. The two-photon microscopic images reveal that the **DCA·NDI-Δ** cocrystal exhibits (Figure 6A) upconversion emission upon excitation at 1000 nm. Its upconversion emission peak centered (Figure 6A and S22) on 640 nm, the value of which is analogous to its one-photon excited fluorescence at 645 nm. The emission intensity shows (Figure 6B and S23) a linear dependence

on the square of incident laser power, suggesting that its upconversion emission originates from a two-photon absorption process.[60,61] **CN·NDI-Δ** cocrystal also displays (Figure 6E and S26) two-photon excited fluorescence with an emission band located at 550 nm (Figure 6D and S25), matching well with its one-photon excited fluorescence centered on 547 nm. **DCA·NDI-Δ** and **CN·NDI-Δ** cocrystals exhibit distinct two-photon excited emission colors, which paves the way for the construction of color-tunable upconversion emission switches.

Two-photon absorption spectra were collected by in-situ two-photon imaging experiments, wherein the incident laser power was fixed at 5.3 mW, and the excitation wavelengths were changed from 700 to 1000 nm. The **DCA·NDI-Δ** cocrystal exhibits (Figure 6C and S24) a broad two-photon absorption with a peak centered on 940 nm. The maximum two-photon absorption of the **CN·NDI-Δ** cocrystal is observed (Figure 6F and S27) at 700 nm, a wavelength which is shorter than that of **DCA·NDI-Δ** cocrystal. Time-dependent density functional theoretical (TDDFT) calculations reveal that **DCA·NDI-Δ** exhibits (Figure S30) a maximum two-photon absorption cross-section (σ_{TPA}) of 239.2 GM at 600 nm, which is higher than that of **CN·NDI-Δ** (65.0 GM at 600 nm). Notably, **DCA·NDI-Δ** displays a strong two-photon absorption band with a maximum σ_{TPA} of 51.0 GM at 1148 nm in the second near-infrared (NIR-II) region, while **CN·NDI-Δ** shows a maximum σ_{TPA} of 53.5 GM at 880 nm in the first near-infrared region. Compared to the **CN·NDI-Δ** cocrystal, **DCA·NDI-Δ** displays a more red-shifted two-photon absorption with absorption bands reaching into the NIR-II region. These results indicate that changing the electron donor of the cocrystals provides an alternative strategy for tuning the nonlinear optical properties of multicomponent crystals.

Commented [GS2]: Where is the data that shows this?

Taking advantage of the cocrystal-to-cocrystal transformation between **DCA·NDI-Δ** and **CN·NDI-Δ** and the different colors of their upconversion fluorescence, a dual-color upconversion emission switch has been achieved. Upon excitation at 1000 nm, the initial **DCA·NDI-Δ** film exhibits (Figures 7A, 7D, 7G, S32 and S35) a red upconversion fluorescence with a peak centered on 640 nm. Upon drop casting of **CN** molecules on the surface of the film, its upconversion emission color changes from red to yellow. The corresponding upconversion emission peak shifts (Figures 7B, 7E and S33) from 640 to 540 nm, an observation which is assigned to the transformation of **DCA·NDI-Δ** to **CN·NDI-Δ** film. The upconversion emission intensity of the transformed **CN·NDI-Δ** film correlates (Figures 7H and S36) linearly with the square of laser power, indicating that its two-photon absorption properties are retained. The transformed **CN·NDI-Δ** film changes back to red-emissive **DCA·NDI-Δ** film after solvent vapor annealing. Its maximum upconversion emission wavelength is red-shifted (Figures 7C,

7F and S34) to 640 nm, and the emission intensity is proportional (Figures 7i and S35) to the square of laser power. These results indicate that the color of two-photon excited fluorescence can be switched between red and yellow by the reversible transformation between **DCA·NDI-Δ** and **CN·NDI-Δ** cocrystals, leading to the formation of a color-tunable upconversion emission switch.

CONCLUSION

A color-tunable upconversion emission switch based on the cocrystal-to-cocrystal transformation has been designed and fabricated. With a naphthalenediimide-based triangular macrocycle **NDI-Δ** as the electron acceptor, two cocrystals **DCA·NDI-Δ** and **CN·NDI-Δ** have been fabricated, which exhibit red and yellow fluorescence, respectively. The red-emissive **DCA·NDI-Δ** cocrystal can transform into a yellow-emissive **CN·NDI-Δ** cocrystal by drop casting of 1-chloronaphthalene molecules, and then recovered by the removal of volatile 1-chloronaphthalene molecules through solvent vapor annealing. Consequently, a reversible cocrystal-to-cocrystal transformation based on the exchange of electron acceptor molecules has been achieved. Attributed to donor-acceptor charge-transfer interactions, the two cocrystals exhibit improved two-photon excited fluorescence. A high-contrast color-tunable upconversion emission switch has been achieved by controlling the transformation of the two cocrystals. This work provides a rare example of precise control of reversible cocrystal transformation based on the exchange of electron donor molecules, realizing the dynamic modulation of superstructures in the crystalline state. It affords an in-depth understanding of the rational design and controlled preparation of multicomponent crystalline materials. Achieving color-tunable upconversion emission in the crystalline state paves the way for the construction of nonlinear optical materials with tunable emissions, promoting the development of solid-state intelligent optical materials and their applications.

EXPERIMENTAL PROCEDURES

Preparation of the DCA·NDI-Δ Cocrystals

NDI-Δ (10.4 mg, 10 μmol) was mixed with **DCA** (2.5 mg, 10 μmol) in CH_2Cl_2 (10 mL) and dissolved by ultrasonic treatment (Figure S1). The solution was filtered with a 0.22-μm syringe filter to remove the insoluble impurities. With slow vapor diffusion of MeOH into the filtered solution, high quality red quadrangle-shaped cocrystals formed after one week.

Preparation of the CN·NDI-Δ Cocrystals

NDI-Δ (10.4 mg, 10 μmol) was first of all dissolved in PhCl (10 mL) by ultrasonic treatment (Figure S2). Then the solution was filtered with a 0.22-μm syringe filter to remove insoluble impurities. **CN** (100 μl) was added to **NDI-Δ** solution. With slow vapor diffusion of MeOH into the PhCl solution (Figure S2), high quality yellow needle-shaped cocrystals formed after one week.

Two-Photon Microscopy

The two-photon absorption-related measurements were carried out on a Nikon A1R-MP$^+$ Multiphoton Microscope equipped with a tunable Chameleon Vision titanium sapphire laser from 700 to 1000 nm. Two-photon absorption spectra were collected by in-situ two-photon imaging experiments, wherein the images were recorded with the laser wavelengths ranging from 700 to 1000 nm and the laser power fixed at 5.3 mW. Two-photon excited fluorescence spectra were performed on a Leica DiveB SP8 Multiphoton Microscope equipped with a Spectra Physics InSight X3 laser. The corresponding two-photon microscopic images were collected at the fixed laser wavelength and laser power, while the fluorescence detection region were varied in the range of 380−780 nm.

Density Functional Theory Computational Methods

The structures from the X-ray single crystals were used for the density functional theory[62] (DFT) calculations in the Amsterdam Density Functional program[63] (ADF, version 2020.102). All-electron single point calculations were performed with the HSE06 functional, a triple zeta basis set[64] with a polarization function (TZP), and Grimme's third generation dispersion with Becke-Johnson damping. The molecular orbitals were visualized with ADFView.

We use second linear response time-dependent density functional theory (SLR-TDDFT) to compute the theoretical two-photon absorption spectra[65,66], and standard linear response TDDFT for the one-photon profiles. Our calculations are "unrelaxed" for computational efficiency, but these agree with relaxed calculations to a very good degree (relaxed simulations are quite computationally demanding for the dimers considered in this work). The PBE0 exchange-correlation functional[67] was employed in our TDDFT application. The Tamm-Dancoff method and the basis set/pseudo-potential SBKJC were used as well. The Davidson threshold used here is 10^{-2}. The two-photon absorption spectra are computed through the well-known sum-over-states formula[68,69] with an intermediate state broadening factor of 0.1 eV and line-shape broadening of 0.2 eV. Due to the very high number of unoccupied orbitals, for the **DCA·NDI-Δ** calculations we ignore virtual orbitals with energies larger than 6.87 eV with respect to the highest-occupied orbital.

Reversible Cocrystal-to-Cocrystal Transformation

The transformation from **DCA·NDI-Δ** film to **CN·NDI-Δ** was induced by employing a drop casting method (Figure S31). The **CN** solution in MeOH (CN/MeOH = 1:9 v/v) was dropped onto the surface of **DCA·NDI-Δ** film. With the evaporation of the droplet, the red **DCA·NDI-Δ** film transforms gradually into the yellow **CN·NDI-Δ** film. The transformed **CN·NDI-Δ** film can recover to **DCA·NDI-Δ** film triggered by solvent vapor annealing (Figure S31).[58] Upon exposure of the transformed **CN·NDI-Δ** film to the vapor of boiling CH_2Cl_2, the film recovers to the initial red **DCA·NDI-Δ** film.

SUPPLEMENTAL INFORMATION

Supplemental Information can be found online at XX.

ACKNOWLEDGMENTS

The authors thank Northwestern University (NU) for its support of this research. LOJ and GCS were supported by NSF grant CHE-2055565This work made use of the IMSERC Crystallography facility at Northwestern University, which has received support from the Soft and Hybrid Nanotechnology Experimental (SHyNE) Resource (NSF ECCS-2025633), and Northwestern University. This work made use of the EPIC facility of Northwestern University's NUANCE Center, which has received support from the SHyNE Resource (NSF ECCS-2025633), the IIN, and Northwestern's MRSEC program (NSF DMR-1720139). The A1R-MP$^+$ multiphoton microscope was acquired through an S10 shared instrumentation grant awarded to Teng-Leong Chew (1 S10 OD010398-01). This work made use of the Northwestern University Center for Advanced Microscopy generously supported by NIH 1S10OD010398-01.

AUTHOR CONTRIBUTIONS

Y.W., H.W. and J.F.S. conceived the idea and led the project. Y.W. and H.W. conducted the experiments and performed the IGM analysis. L.O.J. and G.C.S. conducted DFT calculations and calculated the frontier molecular orbitals. M.A.M. performed the TDDFT calculations and computed the one-photon and two-photon absorption spectra. C.L.S. carried out the X-ray crystallographic analysis. Y.W., H.W. and J.F.S. wrote the first and subsequent drafts of the manuscript. All authors discussed the experimental results and commented on the manuscript.

DECLARATION OF INTERESTS

The authors declare no conflicting interests.

REFERENCES

1. Aitipamula, S., Banerjee, R., Bansal, A.K., Biradha, K., Cheney, M.L., Choudhury, A.R., Desiraju, G.R., Dikundwar, A.G., Dubey, R., Duggirala, N., et al. (2012). Polymorphs, salts, and cocrystals: What's in a name? Cryst. Growth Des. *12*, 2147−2152.

2. Goetz, K.P., Vermeulen, D., Payne, M.E., Kloc, C., McNeil, L.E., and Jurchescu, O.D. (2014). Charge-transfer complexes: New perspectives on an old class of compounds. J. Mater. Chem. C *2*, 3065−3076.

3. Jiang, H., Hu, P., Ye, J., Zhang, K.K., Long, Y., Hu, W., and Kloc, C. (2018). Tuning of the degree of charge transfer and the electronic properties in organic binary compounds by crystal engineering: A perspective. J. Mater. Chem. C *6*, 1884−1902.

4. Little, M.A., Briggs, M.E., Jones, J.T.A., Schmidtmann, M., Hasell, T., Chong, S.Y., Jelfs, K.E., Chen, L., and Cooper, A.I. (2015). Trapping virtual pores by crystal retro-engineering. Nat. Chem. *7*, 153−159.

5. Catalano, L., Pérez-Estrada, S., Terraneo, G., Pilati, T., Resnati, G., Metrangolo, P., and Garcia-Garibay, M.A. (2015). Dynamic characterization of crystalline supramolecular rotors assembled through halogen bonding. J. Am. Chem. Soc. *137*, 15386−15389.

6. Li, M., Hua, B., Liang, H.Z., Liu, J.Y., Shao, L., and Huang, F.H. (2020). Supramolecular tessellations via pillar[n]arenes-based exo-wall interactions. J. Am. Chem. Soc. *142*, 20892−20901.

7. Luo, D., Tian, J., Sessler, J.L., and Chi, X. (2021). Nonporous adaptive calix[4]pyrrole crystals for polar compound separations. J. Am. Chem. Soc. *143*, 18849−18853.

8. Duggirala, N.K., Perry, M.L., Almarsson, O., and Zaworotko, M.J. (2016). Pharmaceutical cocrystals: Along the path to improved medicines. Chem. Commun. *52*, 640−655.

9. Tian, S., Bai, H., Li, S., Xiao, Y., Cui, X., Li, X., Tan, J., Huang, Z., Shen, D., Liu, W., et al. (2021). Water-soluble organic nanoparticles with programable intermolecular charge transfer for NIR-II photothermal anti-bacterial therapy. Angew. Chem. Int. Ed. *60*, 11758−11762.

10. Lei, Y.L., Liao, L.S., and Lee, S.T. (2013). Selective growth of dual-color-emitting heterogeneous microdumbbells composed of organic charge-transfer complexes. J. Am. Chem. Soc. *135*, 3744−3747.

11. Black, H.T., and Perepichka, D.F. (2014). Crystal engineering of dual channel p/n organic semiconductors by complementary hydrogen bonding. Angew. Chem. Int. Ed. *53*, 2138−2142.

12. Ning, G.-H., Cui, P., Sazanovich, I.V., Pegg, J.T., Zhu, Q., Pang, Z., Wei, R.-J., Towrie, M., Jelfs, K.E., Little, M.A., and Cooper, A.I. (2021). Organic cage inclusion crystals exhibiting guest-enhanced multiphoton harvesting. Chem *7*, 3157−3170.

13. Zhang, J., Xu, W., Sheng, P., Zhao, G., and Zhu, D. (2017). Organic donor–acceptor complexes as novel organic semiconductors. Acc. Chem. Res. *50*, 1654−1662.

14. Sun, Y., Lei, Y., Hu, W., and Wong, W.-Y. (2020). Epitaxial growth of nanorod meshes from luminescent organic cocrystals via crystal transformation. J. Am. Chem. Soc. *142*, 7265−7269.

15. Braga, D., Maini, L., and Grepioni, F. (2013). Mechanochemical preparation of co-crystals. Chem. Soc. Rev. *42*, 7638−7648.

16. Wang, Z., Yu, F., Chen, W., Wang, J., Liu, J., Yao, C., Zhao, J., Dong, H., Hu, W., and Zhang, Q. (2020). Rational control of charge transfer excitons toward high-contrast reversible mechanoresponsive luminescent switching. Angew. Chem. Int. Ed. *59*, 17580−17586.

17. Liu, Y.J., Li, A.S., Xu, S.P., Xu, W.Q., Liu, Y., Tian, W.J., and Xu, B. (2020). Reversible luminescent switching in an organic cocrystal: Multi-stimuli-induced crystal-to-crystal phase transformation. Angew. Chem. Int. Ed. *59*, 15098−15103.

18. Yu, P., Zhen, Y., Dong, H., and Hu, W. (2019). Crystal engineering of organic optoelectronic materials. Chem *5*, 2814−2853.

19. Park, S.K., Kim, J.H., and Park, S.Y. (2018). Organic 2D optoelectronic crystals: Charge transport, emerging functions, and their design perspective. Adv. Mater. *30*, 1704759.

20. Huang, Y., Wang, Z., Chen, Z., and Zhang, Q. (2019). Organic cocrystals: Beyond electrical conductivities and field-effect transistors (FETs). Angew. Chem. Int. Ed. *58*, 9696−9711.

21. Sun, L., Wang, Y., Yang, F., Zhang, X., and Hu, W. (2019). Cocrystal engineering: A collaborative strategy toward functional materials. Adv. Mater. *31*, 1902328.

22. Coleman, L.B., Cohen, M.J., Sandman, D.J., Yamagishi, F.G., Garito, A.F., and Heeger, A.J. (1973). Superconducting fluctuations and the peierls instability in an organic solid. Solid State Commun. *12*, 1125−1132.

23. Park, S.K., Kim, J.H., Ohto, T., Yamada, R., Jones, A.O.F., Whang, D.R., Cho, I., Oh, S., Hong, S.H., Kwon, J.E., et al. (2017). Highly luminescent 2D-type slab crystals based on a molecular charge-transfer complex as promising organic light-emitting transistor materials. Adv. Mater. *29*, 1701346.

24. Tayi, A.S., Shveyd, A.K., Sue, A.C.H., Szarko, J.M., Rolczynski, B.S., Cao, D., Kennedy, T.J., Sarjeant, A.A., Stern, C.L., Paxton, W.F., et al. (2012). Room-temperature ferroelectricity in supramolecular networks of charge-transfer complexes. Nature *488*, 485−489.

25. Shin, M.H., Lee, S.H., Kang, B.J., Jazbinsek, M., Yoon, W., Yun, H., Rotermund, F., and Kwon, O.P. (2018). Organic three-component single crystals with pseudo-isomorphic cocrystallization for nonlinear optics and THz photonics. Adv. Funct. Mater. *28*, 1805257.
26. Bolton, O., Lee, K., Kim, H.J., Lin, K.Y., and Kim, J. (2011). Activating efficient phosphorescence from purely organic materials by crystal design. Nat. Chem. *3*, 205−210.
27. Park, S.K., Cho, I., Gierschner, J., Kim, J.H., Kim, J.H., Kwon, J.E., Kwon, O.K., Whang, D.R., Park, J.-H., An, B.-K., and Park, S.Y. (2016). Stimuli-responsive reversible fluorescence switching in a crystalline donor-acceptor mixture film: Mixed stack charge-transfer emission versus segregated stack monomer emission. Angew. Chem. Int. Ed. *55*, 203−207.
28. Liu, G., Liu, J., Ye, X., Nie, L., Gu, P., Tao, X., and Zhang, Q. (2017). Self-healing behavior in a thermo-mechanically responsive cocrystal during a reversible phase transition. Angew. Chem. Int. Ed. *56*, 198−202.
29. Liu, Y., Zeng, Q., Zou, B., Liu, Y., Xu, B., and Tian, W. (2018). Piezochromic luminescence of donor-acceptor cocrystals: Distinct responses to anisotropic grinding and isotropic compression. Angew. Chem. Int. Ed. *57*, 15670−15674.
30. Borchers, T.H., Topić, F., Christopherson, J.C., Bushuyev, O.S., Vainauskas, J., Titi, H.M., Friščić, T., and Barrett, C.J. (2022). Cold photo-carving of halogen-bonded co-crystals of a dye and a volatile co-former using visible light. Nat. Chem. *14*, 574−581.
31. Zhao, W., He, Z., and Tang, B.Z. (2020). Room-temperature phosphorescence from organic aggregates. Nat. Rev. Mater. *5*, 869−885.
32. Zhuo, M.-P., Yuan, Y., Su, Y., Chen, S., Chen, Y.-T., Feng, Z.-Q., Qu, Y.-K., Li, M.-D., Li, Y., Hu, B.-W., et al. (2022). Segregated array tailoring charge-transfer degree of organic cocrystal for the efficient near-infrared emission beyond 760 nm. Adv. Mater. *34*, 2107169.
33. Li, S.Z., Lu, B., Fang, X.Y., and Yan, D.P. (2020). Manipulating light-induced dynamic macro-movement and static photonic properties within 1D isostructural hydrogen-bonded molecular cocrystals. Angew. Chem. Int. Ed. *59*, 22623−22630.
34. Varughese, S. (2014). Non-covalent routes to tune the optical properties of molecular materials. J. Mater. Chem. C *2*, 3499−3516.
35. Deng, R., Qin, F., Chen, R., Huang, W., Hong, M., and Liu, X. (2015). Temporal full-colour tuning through non-steady-state upconversion. Nat. Nanotechnol. *10*, 237−242.
36. Massaro, G., Hernando, J., Ruiz-Molina, D., Roscini, C., and Latterini, L. (2016). Thermally switchable molecular upconversion emission. Chem. Mater. *28*, 738−745.
37. Yao, W., Tian, Q., and Wu, W. (2019). Tunable emissions of upconversion fluorescence for security applications. Adv. Optical Mater. *7*, 1801171.

38. Wu, Y., Xu, J., Qin, X., Xu, J., and Liu, X. (2021). Dynamic upconversion multicolour editing enabled by molecule-assisted opto-electrochemical modulation. Nat. Commun. *12*, 2022.

39. Yan, D., Delori, A., Lloyd, G.O., Friscic, T., Day, G.M., Jones, W., Lu, J., Wei, M., Evans, D.G., and Duan, X. (2011). A cocrystal strategy to tune the luminescent properties of stilbene-type organic solid-state materials. Angew. Chem. Int. Ed. *50*, 12483−12486.

40. Wang, Y., Wu, H., Li, P., Chen, S., Jones, L.O., Mosquera, M.A., Zhang, L., Cai, K., Chen, H., Chen, X.-Y., et al. (2020). Two-photon excited deep-red and near-infrared emissive organic co-crystals. Nat. Commun. *11*, 4633.

41. Bai, L., Bose, P., Gao, Q., Li, Y., Ganguly, R., and Zhao, Y. (2017). Halogen-assisted piezochromic supramolecular assemblies for versatile haptic memory. J. Am. Chem. Soc. *139*, 436−441.

42. Lei, Y.-L., Jin, Y., Zhou, D.-Y., Gu, W., Shi, X.-B., Liao, L.-S., and Lee, S.-T. (2012). White-light emitting microtubes of mixed organic charge-transfer complexes. Adv. Mater. *24*, 5345−5351.

43. Zhou, B., Yan, L., Huang, J., Liu, X., Tao, L., and Zhang, Q. (2020). NIR II-responsive photon upconversion through energy migration in an ytterbium sublattice. Nat. Photon. *14*, 760−766.

44. Zhang, J., Li, A., Zou, H., Peng, J., Guo, J., Wu, W., Zhang, H., Zhang, J., Gu, X., Xu, W., et al. (2020). A “simple” donor–acceptor AIEgen with multi-stimuli responsive behavior. Mater. Horiz. *7*, 135−142.

45. Zhang, C., Zhou, H.P., Liao, L.Y., Feng, W., Sun, W., Li, Z.X., Xu, C.H., Fang, C.J., Sun, L.D., Zhang, Y.W., and Yan, C.H. (2010). Luminescence modulation of ordered upconversion nanopatterns by a photochromic diarylethene: Rewritable optical storage with nondestructive readout. Adv. Mater. *22*, 633−637.

46. Mase, K., Sasaki, Y., Sagara, Y., Tamaoki, N., Weder, C., Yanai, N., and Kimizuka, N. (2018). Stimuli-responsive dual-color photon upconversion: A singlet-to-triplet absorption sensitizer in a soft luminescent cyclophane. Angew. Chem. Int. Ed. *57*, 2806−2810.

47. Chen, G., Qiu, H., Prasad, P.N., and Chen, X. (2014). Upconversion nanoparticles: Design, nanochemistry, and applications in theranostics. Chem. Rev. *114*, 5161−5214.

48. Schneebeli, S.T., Frasconi, M., Liu, Z., Wu, Y., Gardner, D.M., Strutt, N.L., Cheng, C., Carmieli, R., Wasielewski, M.R., and Stoddart, J.F. (2013). Electron sharing and anion–π recognition in molecular triangular prisms. Angew. Chem. Int. Ed. *52*, 13100−13104.

49. Beldjoudi, Y., Narayanan, A., Roy, I., Pearson, T.J., Cetin, M.M., Nguyen, M.T., Krzyaniak, M.D., Alsubaie, F.M., Wasielewski, M.R., Stupp, S.I., and Stoddart, J.F. (2019). Supramolecular tessellations by a rigid naphthalene diimide triangle. J. Am. Chem. Soc. *141*, 17783–17795.

50. Wang, Y., Wu, H., and Stoddart, J.F. (2021). Molecular triangles: A new class of macrocycles. Acc. Chem. Res. *54*, 2027−2039.

51. Vadehra, G.S., Maloney, R.P., Garcia-Garibay, M.A., and Dunn, B. (2014). Naphthalene diimide based materials with adjustable redox potentials: Evaluation for organic lithium-ion batteries. Chem. Mater. *26*, 7151−7157.

52. Suraru, S.L., and Wurthner, F. (2014). Strategies for the synthesis of functional naphthalene diimides. Angew. Chem. Int. Ed. *53*, 7428−7448.

53. Makarov, N.S., Drobizhev, M., and Rebane, A. (2008). Two-photon absorption standards in the 550–1600 nm excitation wavelength range. Opt. Express *16*, 4029−4047.

54. Uejima, M., Sato, T., Tanaka, K., and Kaji, H. (2014). Enhancement of fluorescence in anthracene by chlorination: Vibronic coupling and transition dipole moment density analysis. Chem. Phys. *430*, 47−55.

55. Monson, P.R., and McClain, W.M. (1972). Complete polarization study of the two-photon absorption of liquid 1-chloronaphthalene. J. Chem. Phys. *56*, 4817−4825.

56. Lu, T., and Chen, F. (2012). Multiwfn: A multifunctional wavefunction analyzer. J. Comput. Chem. *33*, 580−592.

57. Lefebvre, C., Rubez, G., Khartabil, H., Boisson, J.-C., Contreras-García, J., and Hénon, E. (2017). Accurately extracting the signature of intermolecular interactions present in the NCI plot of the reduced density gradient versus electron density. Phys. Chem. Chem. Phys. *19*, 17928−17936.

58. Liu, C., Minari, T., Lu, X., Kumatani, A., Takimiya, K., and Tsukagoshi, K. (2011). Solution-processable organic single crystals with bandlike transport in field-effect transistors. Adv. Mater. *23*, 523−526.

59. Sun, L., Zhu, W., Wang, W., Yang, F., Zhang, C., Wang, S., Zhang, X., Li, R., Dong, H., and Hu, W. (2017). Intermolecular charge-transfer interactions facilitate two-photon absorption in styrylpyridine-tetracyanobenzene cocrystals. Angew. Chem. Int. Ed. *56*, 7831−7835.

60. Pawlicki, M., Collins, H.A., Denning, R.G., and Anderson, H.L. (2009). Two-photon absorption and the design of two-photon dyes. Angew. Chem. Int. Ed. *48*, 3244−3266.

61. Drobizhev, M., Makarov, N.S., Tillo, S.E., Hughes, T.E., and Rebane, A. (2011). Two-photon absorption properties of fluorescent proteins. Nat. Methods *8*, 393−399.

62. Versluis, L., and Ziegler, T. (1988). The determination of molecular structures by density functional theory. The evaluation of analytical energy gradients by numerical integration. J. Chem. Phys. *88*, 322−328.
63. te Velde, G., Bickelhaupt, F.M., Baerends, E.J., Fonseca Guerra, C., van Gisbergen, S.J.A., Snijders, J.G., and Ziegler, T. (2001). Chemistry with ADF. J. Comput. Chem. *22*, 931−967.
64. Van Lenthe, E., and Baerends, E.J. (2003). Optimized slater-type basis sets for the elements 1–118. J. Comput. Chem. *24*, 1142−1156.
65. Mosquera, M.A., Chen, L.X., Ratner, M.A., and Schatz, G.C. (2016). Sequential double excitations from linear-response time-dependent density functional theory. J. Chem. Phys. *144*, 204105.
66. Mosquera, M.A., Jones, L.O., Kang, G., Ratner, M.A., and Schatz, G.C. (2021). Second linear response theory and the analytic calculation of excited-state properties. J. Phys. Chem. A *125*, 1093−1102.
67. Adamo, C., and Barone, V. (1999). Toward reliable density functional methods without adjustable parameters: The PBE0 model. J. Chem. Phys. *110*, 6158−6170.
68. Silva, D.L., Krawczyk, P., Bartkowiak, W., and Mendonça, C.R. (2009). Theoretical study of one- and two-photon absorption spectra of azoaromatic compounds. J. Chem. Phys. *131*, 244516.
69. Ohta, K., Antonov, L., Yamada, S., and Kamada, K. (2007). Theoretical study of the two-photon absorption properties of several asymmetrically substituted stilbenoid molecules. J. Chem. Phys. *127*, 084504.

Captions to Scheme and Figures

Scheme 1. Schematic illustration of cocrystal-to-cocrystal transformation and structural formulas of NDI-Δ, DCA, and CN. Two cocrystals **DCA·NDI-Δ** and **CN·NDI-Δ** can undergo reversible transformation based on the exchange of electron donor molecules.

Figure 1. Microscopy images and solid-state photophysical properties of DCA·NDI-Δ and CN·NDI-Δ cocrystals. (A) Optical microscopy and corresponding fluorescence microscopy images of **DCA·NDI-Δ** cocrystals. (B) Optical microscopy and corresponding fluorescence microscopy images of **CN·NDI-Δ** cocrystals. (C) Solid-state UV-Vis absorption spectra of **NDI-Δ**, **DCA**, **CN·NDI-Δ** and **DCA·NDI-Δ**. (D) Solid-state fluorescence spectra of **NDI-Δ**, **DCA**, **CN·NDI-Δ** and **DCA·NDI-Δ**.

Figure 2. Solid-state superstructure of DCA·NDI-Δ cocrystal. (A) Plan view of a capped-sticks representation showing the face-to-face packing between **DCA** and **NDI-Δ** molecules. (B) Side-on view of a capped-sticks representation demonstrating that two adjacent **NDI-Δ** macrocycles are connected by [C−H···O] hydrogen bonding. (C) Visualized intermolecular binding iso-surface between **DCA** and **NDI-Δ** molecules. (D) Visualized intermolecular binding iso-surface between two adjacent **NDI-Δ** macrocycles. (E) Solid-state superstructure of **DCA·NDI-Δ** cocrystal illustrating that **DCA** molecules and **NDI-Δ** macrocycles stack into a hexagonal superstructure.

Figure 3. Solid-state superstructure of CN·NDI-Δ cocrystal. (A) Plan view of a capped-sticks representation showing the face-to-face packing between **CN** and **NDI-Δ** molecules. (B) Side-on view of a capped-sticks representation demonstrating that two adjacent **NDI-Δ** macrocycles are connected by [C−H···O] hydrogen bonding. (C) Visualized intermolecular binding iso-surface between **CN** and **NDI-Δ** molecules. (D) Visualized intermolecular binding iso-surface between two adjacent **NDI-Δ** macrocycles. (E) Solid-state superstructure of **CN·NDI-Δ** cocrystal illustrating that **CN** and **NDI-Δ** molecules assemble into a vertex-to-edge tiling pattern.

Figure 4. Frontier molecular orbital calculations. HOMO and LUMO frontier molecular orbitals of **DCA**, **DCA·NDI-Δ**, **CN·NDI-Δ** and **CN**.

Figure 5. Reversible Cocrystal-to-Cocrystal Transformation. (A) Schematic illustration of cocrystal transformation between **DCA·NDI-Δ** and **CN·NDI-Δ**. Step (i) represents introducing **CN** molecules by drop casting. Step (ii) means removing **CN** molecules by solvent vapor

annealing. (B) Fluorescence microscopy image of initial **DCA·NDI-Δ** film. (C) Fluorescence microscopy image of transformed **CN·NDI-Δ** film. (D) Fluorescence microscopy image of recovered **DCA·NDI-Δ** film. (E) Fluorescence spectrum of initial **DCA·NDI-Δ** film. (F) Fluorescence spectrum of transformed **CN·NDI-Δ** film. (G) Fluorescence spectrum of recovered **DCA·NDI-Δ** film. (H) Powder X-ray diffraction patterns of **CN·NDI-Δ** cocrystal, initial **DCA·NDI-Δ** film, transformed **CN·NDI-Δ** film, and recovered **DCA·NDI-Δ** film, showing that cocrystal transformation is reversible. (I) Raman spectra of **CN·NDI-Δ** cocrystal, initial **DCA·NDI-Δ** film, transformed **CN·NDI-Δ** film, and recovered **DCA·NDI-Δ** film.

Figure 6. Photon upconversion properties of DCA·NDI-Δ and CN·NDI-Δ cocrystals. (A) Two-photon excited fluorescence spectrum of **DCA·NDI-Δ** cocrystal excited at 1000 nm. (B) Excitation power dependence of upconversion emission intensity for **DCA·NDI-Δ** cocrystal excited at 1000 nm. (C) Two-photon absorption spectrum of **DCA·NDI-Δ** cocrystal measured with a constant laser power of 5.3 mW. (D) Two-photon excited fluorescence spectrum of **CN·NDI-Δ** cocrystal excited at 800 nm. (E) Excitation power dependence of upconversion emission intensity for **CN·NDI-Δ** cocrystal excited at 700 nm. (F) Two-photon absorption spectrum of **CN·NDI-Δ** cocrystal measured with a constant laser power of 5.3 mW. The insets are the two-photon microscopy images of each cocrystal sample.

Figure 7. Reversible Upconversion Emission Switch. (A) Two-photon microscopy image of initial **DCA·NDI-Δ**. (B) Two-photon microscopy image of transformed **CN·NDI-Δ** film. (C) Two-photon microscopy image of recovered **DCA·NDI-Δ** film. Step (i) represents introducing **CN** molecules by drop casting. Step (ii) means removing **CN** molecules by solvent vapor annealing. (D) Two-photon excited fluorescence spectrum of initial **DCA·NDI-Δ** film. (E) Two-photon excited fluorescence spectrum of transformed **CN·NDI-Δ** film. (F) Two-photon excited fluorescence spectrum of recovered **DCA·NDI-Δ** film. (G) Excitation power dependence of upconversion emission intensity for initial **DCA·NDI-Δ** film excited at 1000 nm. (H) Excitation power dependence of upconversion emission intensity for transformed **CN·NDI-Δ** film excited at 700 nm. (I) Excitation power dependence of upconversion emission intensity for recovered **DCA·NDI-Δ** film excited at 1000 nm.

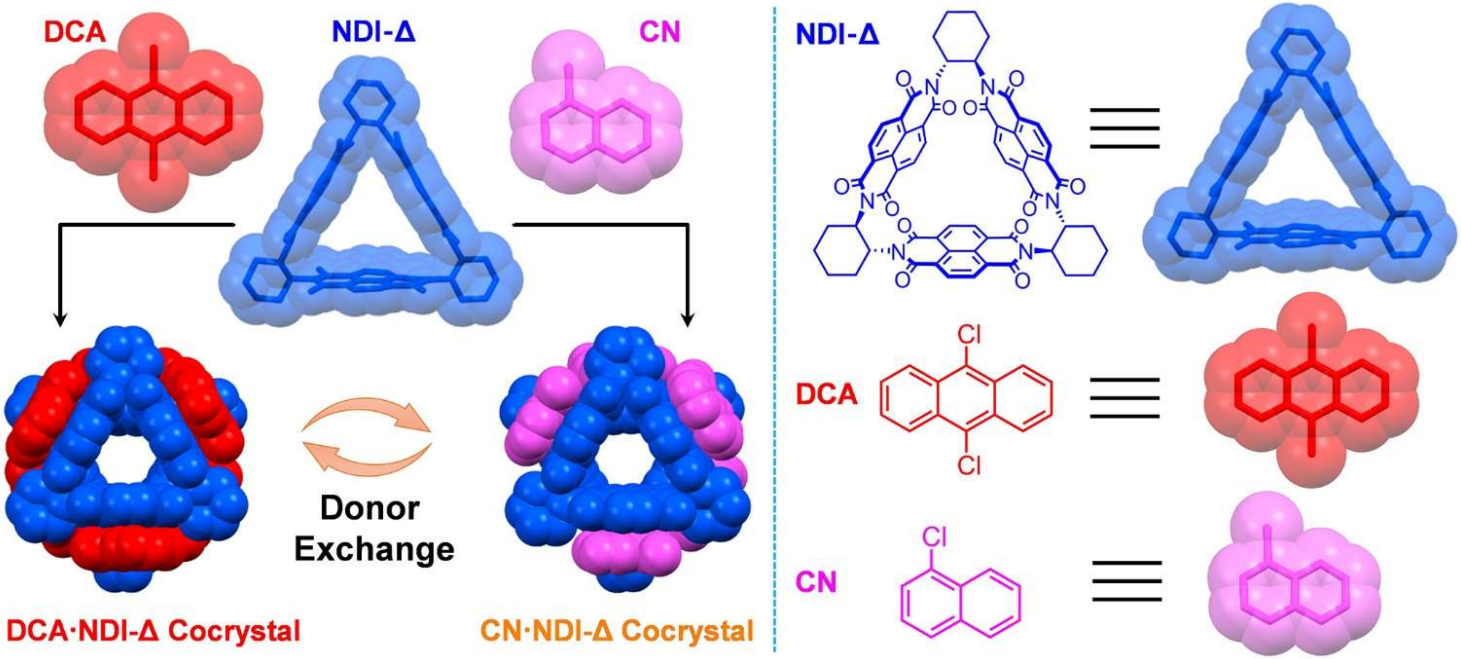
DCA
NDI-Δ
CN
Donor
Exchange
DCA·NDI-Δ Cocrystal
CN·NDI-Δ Cocrystal
NDI-Δ
DCA
Cl
Cl
CN
Cl

Scheme 1

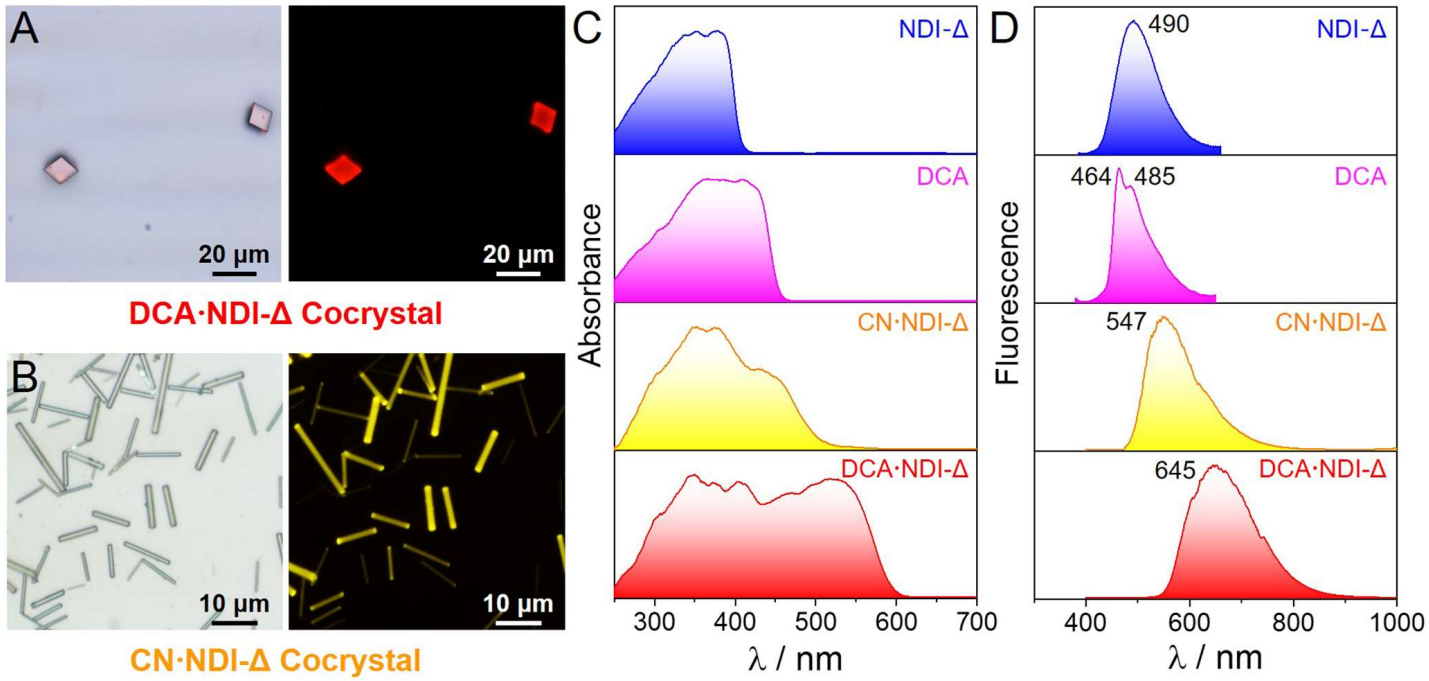
A
20 μm
20 μm
DCA·NDI-Δ Cocrystal
B
10 μm
10 μm
CN·NDI-Δ Cocrystal
C
NDI-Δ
DCA
CN·NDI-Δ
DCA·NDI-Δ
Absorbance
300
400
500
600
700
λ / nm
D
490
NDI-Δ
464
485
DCA
547
CN·NDI-Δ
645
DCA·NDI-Δ
Fluorescence
400
600
800
1000
λ / nm

Figure 1

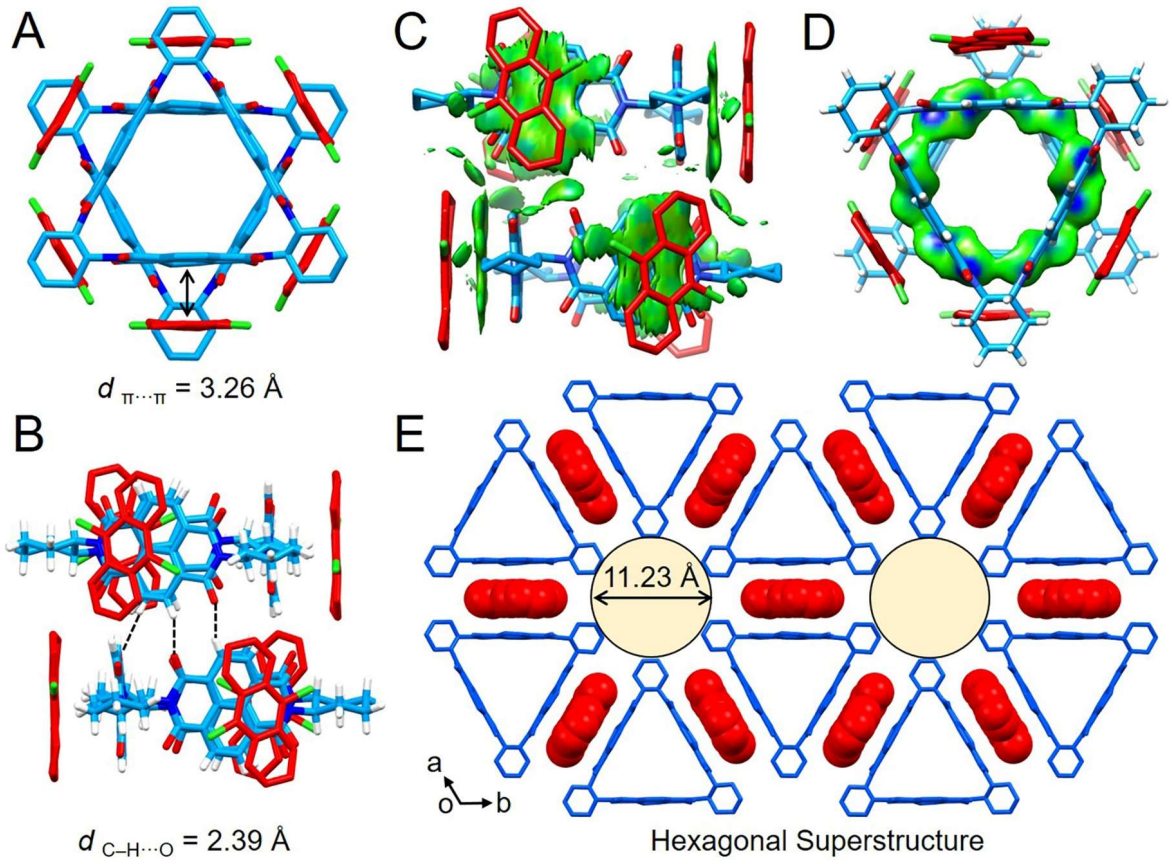
A
C
D
$d_{\pi\cdots\pi}$ = 3.26 Å
B
E
11.23 Å
a
o
b
$d_{C-H\cdots O}$ = 2.39 Å
Hexagonal Superstructure

Figure 2

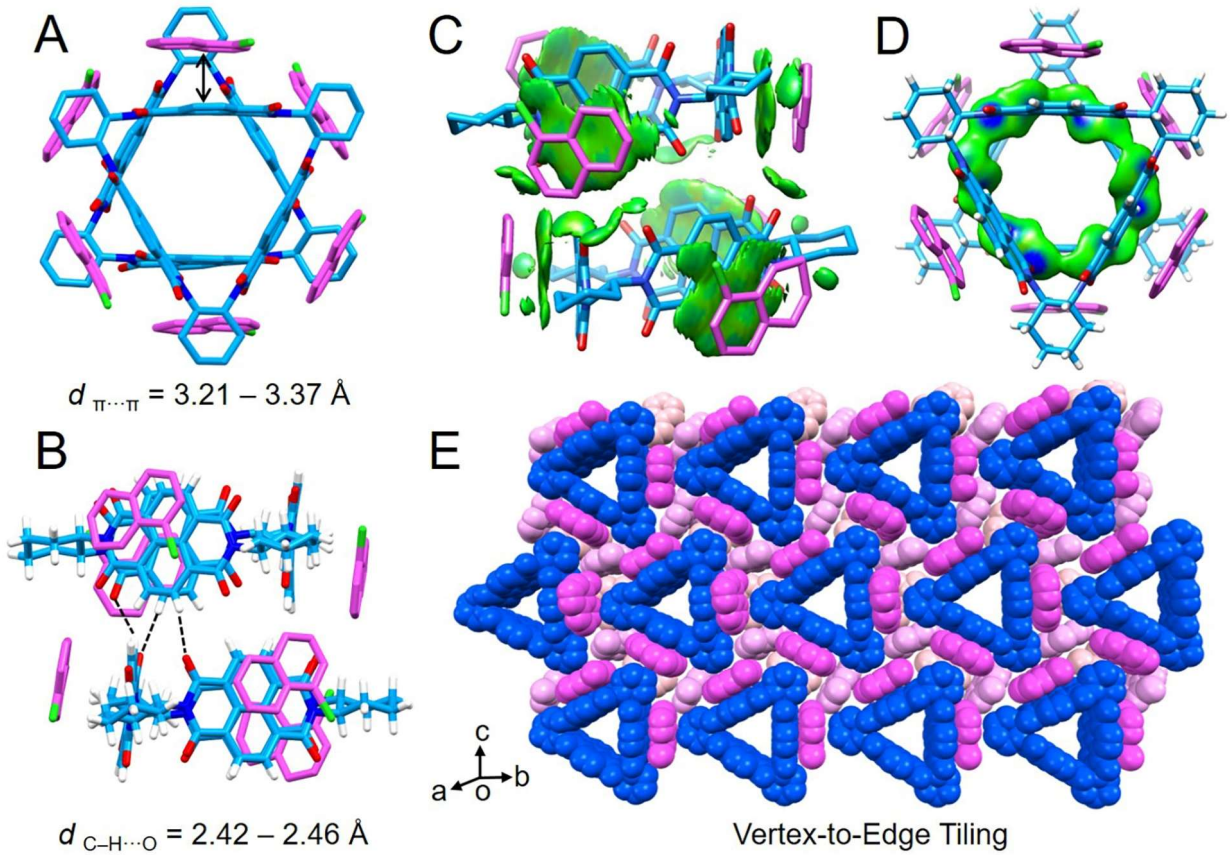
A
C
D
$d_{\pi\cdots\pi}$ = 3.21 – 3.37 Å
B
E
c
a
o
b
$d_{C-H\cdots O}$ = 2.42 – 2.46 Å
Vertex-to-Edge Tiling

Figure 3

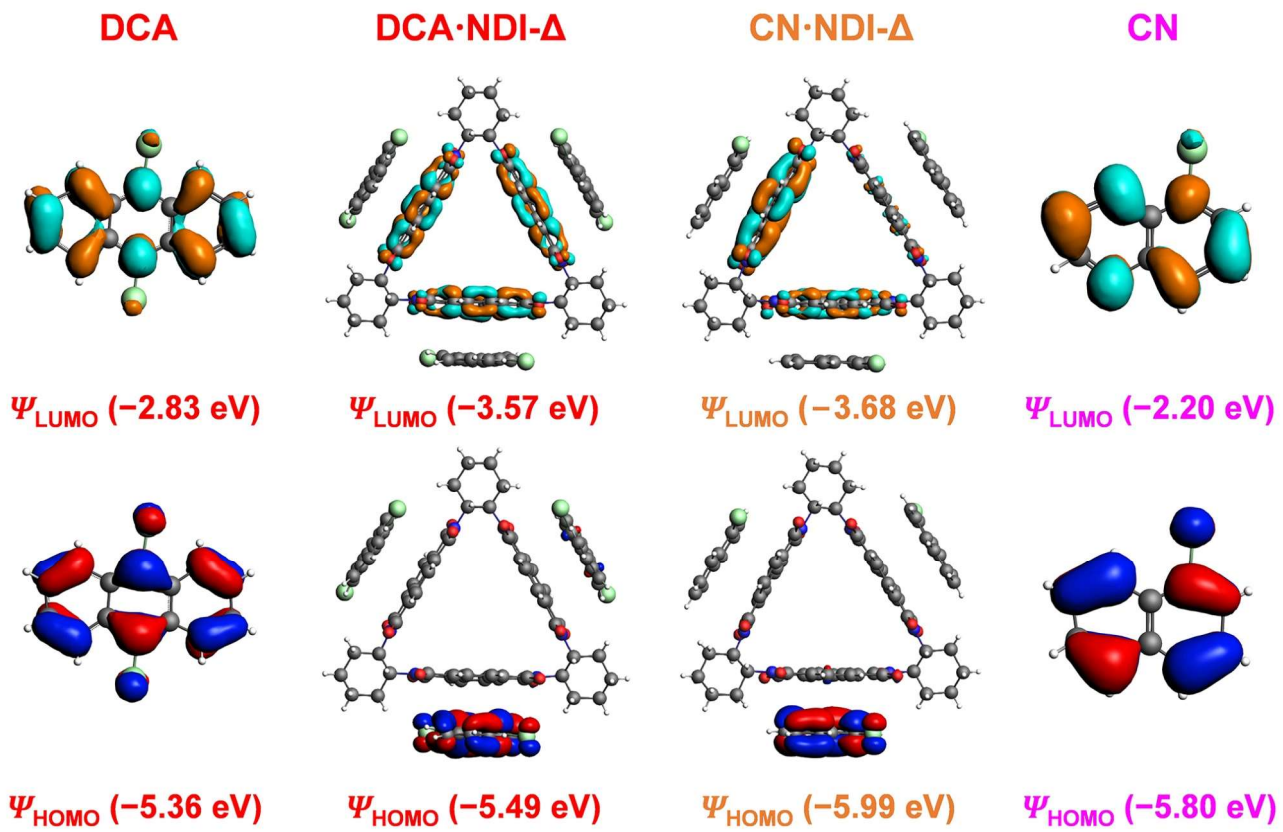
DCA
DCA·NDI-Δ
CN·NDI-Δ
CN
Ψ_{LUMO} (−2.83 eV)
Ψ_{LUMO} (−3.57 eV)
Ψ_{LUMO} (−3.68 eV)
Ψ_{LUMO} (−2.20 eV)
Ψ_{HOMO} (−5.36 eV)
Ψ_{HOMO} (−5.49 eV)
Ψ_{HOMO} (−5.99 eV)
Ψ_{HOMO} (−5.80 eV)

Figure 4

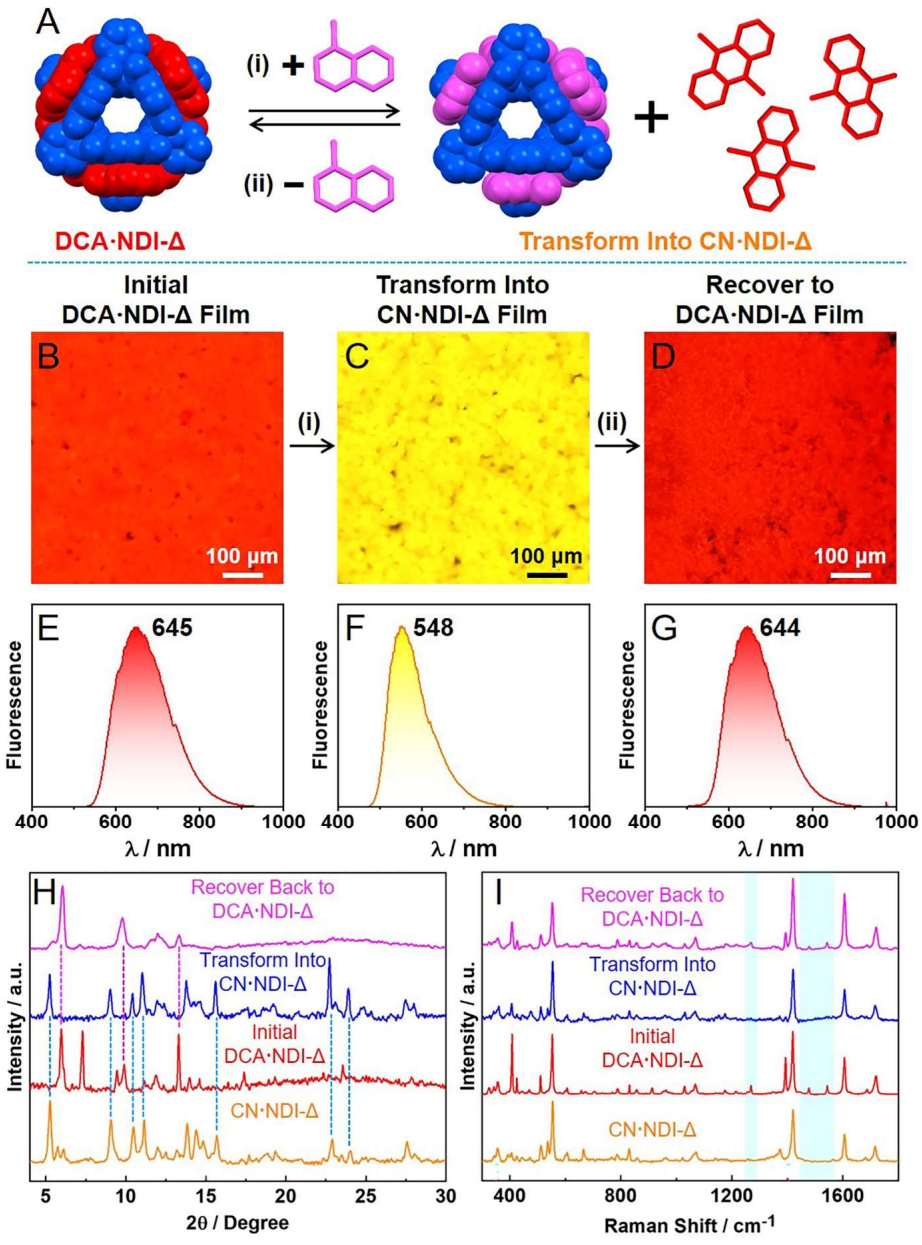
A
(i) +
(ii) −
DCA·NDI-Δ
Transform Into CN·NDI-Δ
Initial
DCA·NDI-Δ Film
Transform Into
CN·NDI-Δ Film
Recover to
DCA·NDI-Δ Film
B
C
D
(i)
(ii)
100 μm
100 μm
100 μm
E
645
F
548
G
644
Fluorescence
λ / nm
H
Recover Back to
DCA·NDI-Δ
Transform Into
CN·NDI-Δ
Initial
DCA·NDI-Δ
CN·NDI-Δ
Intensity / a.u.
2θ / Degree
I
Raman Shift / cm-1

Figure 5

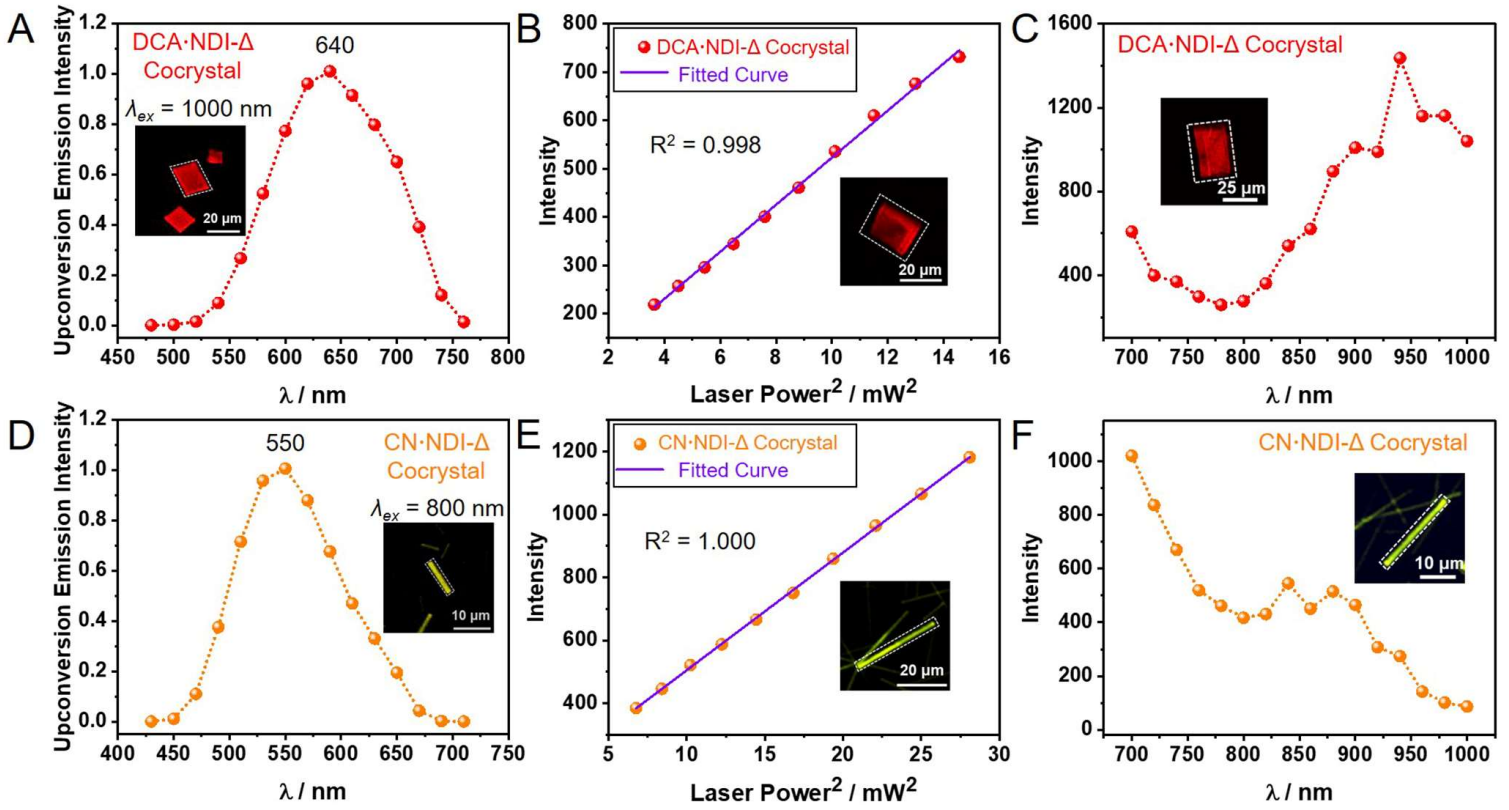
A
DCA·NDI-Δ
Cocrystal
640
λ_{ex} = 1000 nm
20 μm
Upconversion Emission Intensity
λ / nm
B
DCA·NDI-Δ Cocrystal
Fitted Curve
R^2 = 0.998
20 μm
Intensity
Laser Power^2 / mW^2
C
DCA·NDI-Δ Cocrystal
25 μm
Intensity
λ / nm
D
550
CN·NDI-Δ
Cocrystal
λ_{ex} = 800 nm
10 μm
Upconversion Emission Intensity
λ / nm
E
CN·NDI-Δ Cocrystal
Fitted Curve
R^2 = 1.000
20 μm
Intensity
Laser Power^2 / mW^2
F
CN·NDI-Δ Cocrystal
10 μm
Intensity
λ / nm

Figure 6

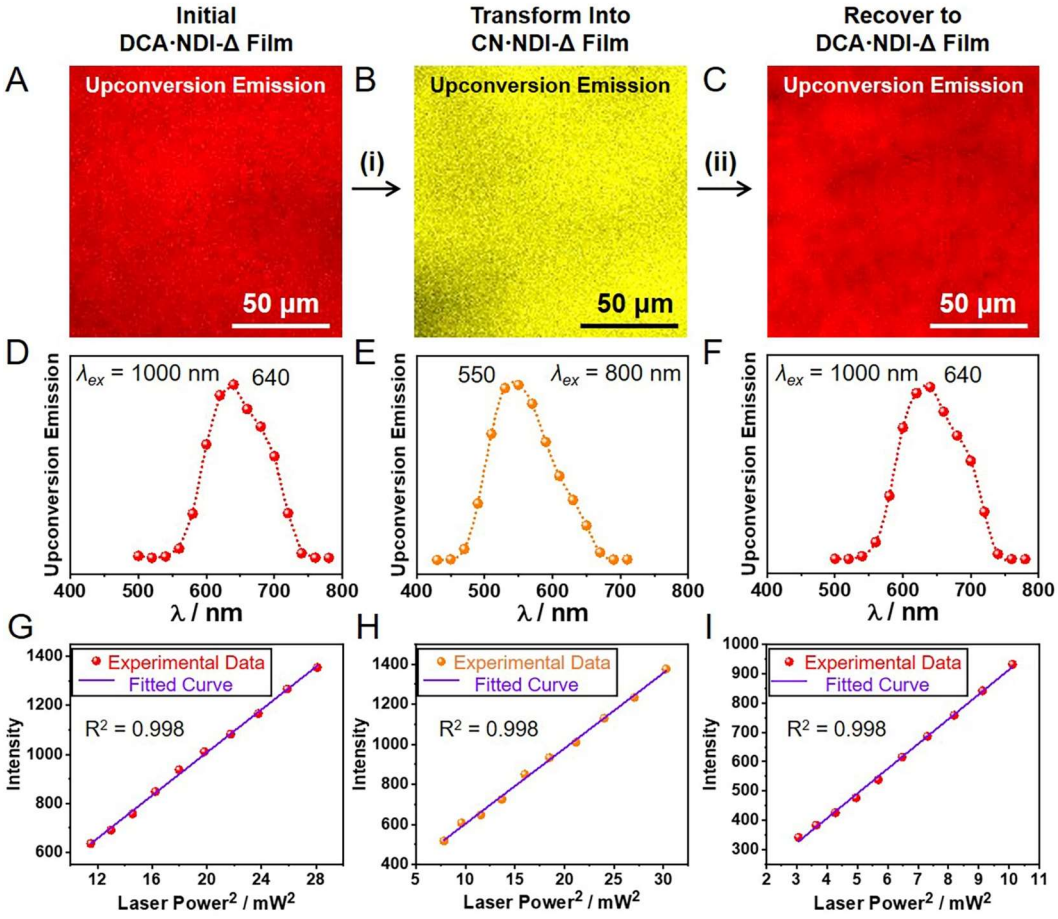
Initial
DCA·NDI-Δ Film
Transform Into
CN·NDI-Δ Film
Recover to
DCA·NDI-Δ Film
A
Upconversion Emission
50 μm
(i)
B
Upconversion Emission
50 μm
(ii)
C
Upconversion Emission
50 μm
D
λex = 1000 nm
640
E
550
λex = 800 nm
F
λex = 1000 nm
640
Upconversion Emission
λ / nm
G
H
I
Experimental Data
Fitted Curve
R2 = 0.998
Intensity
Laser Power2 / mW2

Figure 7

For Table of Contents Only